Reversed Electron Transfer in Dual Single Atom Catalyst for Boosted Photoreduction of CO_2

Yanzhao Zhang, Bernt Johannessen, Peng Zhang, Jinlong Gong, Jingrun Ran,* and Shi-Zhang Qiao*

Photogenerated charge localization on material surfaces significantly affects photocatalytic performance, especially for multi-electron CO_2 reduction. Dual single atom (DSA) catalysts with flexibly designed reactive sites have received significant research attention for CO_2 photoreduction. However, the charge transfer mechanism in DSA catalysts remains poorly understood. Here, for the first time, a reversed electron transfer mechanism on Au and Co DSA catalysts is reported. In situ characterizations confirm that for CdS nanoparticles (NPs) loaded with Co or Au single atoms, photogenerated electrons are localized around the single atom of Co or Au. In DSA catalysts, however, electrons are delocalized from Au and accumulate around Co atoms. Importantly, combined advanced spectroscopic findings and theoretical computation evidence that this reversed electron transfer in Au/Co DSA boosts charge redistribution and activation of CO_2 molecules, leading to highly significantly increased photocatalytic CO_2 reduction, for example, Au/Co DSA loaded CdS exhibits, respectively, $\approx$2800% and 700% greater yields for CO and CH_4 compared with that for CdS alone. Reversed electron transfer in DSA can be used for practical design for charge redistribution and to boost photoreduction of CO_2. Findings will be of benefit to researchers and manufacturers in DSA-loaded catalysts for the generation of solar fuels.

Y. Zhang, J. Ran, S.-Z. Qiao
School of Chemical Engineering
The University of Adelaide
Adelaide, South Australia 5005, Australia
E-mail: jingrun.ran@adelaide.edu.au; s.qiao@adelaide.edu.au
B. Johannessen
Australian Synchrotron
800 Blackburn Rd, Clayton, Victoria 3168, Australia
P. Zhang, J. Gong
Key Laboratory for Green Chemical Technology of Ministry of Education,
School of Chemical Engineering & Technology
Tianjin University
Collaborative Innovation Center of Chemical Science and Engineering
Tianjin 300072, China

1. Introduction

Photocatalytic carbon dioxide (CO_2) reduction reaction is attractive for solar-to-fuels conversion and carbon neutrality.[1–5] However, current performance for CO_2 photoreduction is considered unsatisfactory because of the following two reasons.[1] First, the inertness of the CO_2 molecule; non-electric dipoles, and strong C=O double bonds limit adsorption and activation.[6,7] Secondly, the intrinsic multi-electron process requires greater electron accumulation and utilization.[8] The creation of electron localization and delocalization therefore for surface electron redistribution to interact with C or O atoms in CO_2 molecules favors breaking the electronic structure symmetry of linear CO_2. Advantageously, the length and angle of C=O bonds can then be changed and CO_2 molecule is activated. Moreover, localized electrons provide sufficient electrons for CO_2 reduction.[8,9]

A number of surface modification strategies including the introduction of surface defects,[10–16] grafted groups,[17,18] and heterogeneous metal atoms,[19–24] have been reported to redistribute electrons and activate CO_2 molecules. Among these, metal sites are of interest because surface electron distribution can be flexibly adjusted via phase/size engineering.[8,25–32] These are however significantly affected by the element, coordinated environment, substrate types, and space of active atoms.[31,32] For example, Pd nanoparticles (NPs) accept electrons from TiO_2 nanosheets via acting as an electron reservoir to boost charge separation/transfer.[33] With the size of metal nanoparticles reduced to a single atom (SA) however, the impact of metal sites and mechanism of electron transfer/distribution becomes more complex.[30,34,35] For instance, contrary to that for Pd NPs, Pd SA reversed electron transfer direction and donated the electron to the supporting TiO_2 nanosheets.[33] In situ X-ray photoelectron spectroscopy (XPS) evidenced that Pt SA attracts electrons from the hosting semiconductor and accumulates electrons for reduction.[36] Moreover, the matrix also impacts the photo-generated electron transfer direction. For example, surface electron density and transfer direction can be modulated via the different types of vacancies on CdS NPs.[8] These findings established that different metal sites and matrixes induce opposite electron flows, resulting in different

**ADVANCED
SCIENCE NEWS**

www.advancedsciencenews.com

**ADVANCED
MATERIALS**

www.advmat.de

regions where electrons are localized or delocalized.[37] A question then is what is the ability to promote the surface electron separation/transfer/accumulation via modulating the electron flow between SAs toward desired reactions including, for example, CO_2 reduction.

DSA-loaded catalysts can be used to establish tunable atomic configurations to modify electron distribution via asymmetric atomic sites.[38–41] Significantly, reported findings about DSAs, e.g., Ni/Cu,[42] Ni/Fe,[43] and Ir/Fe[44] systems, highlight the importance of incorporating heterogeneous atomic sites, namely, 1) optimizing the reaction thermodynamics, 2) improve reaction kinetics, and 3) modulating electronic interactions between atoms for complex surface redox reactions. There are however reported findings on modulating the charge distribution between heterogeneous atomic sites as practically challenging to establish charge dynamics in photocatalysts, especially the charge transfer mechanism in DSA-loaded catalysts. Confirmation of a distinct DSA system loaded on a matrix in which one type of SA localizes electrons for reduction while the other delocalizes electrons to boost the enrichment of electrons, are therefore of potential practical significance.

Here, we report the design and evaluation of Au/Co DSA-loaded CdS NPs for the first time. We confirm a mechanism for surface photo-generated electron/hole redistribution for CO_2 conversion via judiciously combined in situ characterizations and theoretical computation. We show that compared with Au or Co SA alone, Au and Co atoms in the DSA system, respectively, delocalize and localize electrons. We evidence that the electron-rich Co atoms more readily adsorb/activate CO_2 molecules to significantly boost photocatalytic CO_2 reduction and charge accumulation and depletion area via in situ tests and calculations. It is concluded that reversed electron transfer in DSA can be used for practical design to boost photoreduction of CO_2. Findings will be of benefit to researchers and manufacturers in the design of DSA-loaded catalysts for solar fuel generation.

2. Results and Discussion

CdS was selected as the matrix material because of its facile synthesis and excellent photocatalytic performance. Co SA loaded CdS NPs are denoted as, respectively, CC1 and CC2, based on Co loading. Au SA-loaded CdS NPs are denoted as CA1 and CA2, respectively, because of different Au loading. Au/Co DSAs loaded CdS NPs are denoted as, respectively, CAC1, CAC2, CAC3, and CAC4, because of differing Au, or Co loading. Details for the synthesis of the catalysts are given in Supporting Information. The SA/DSA catalysts were assessed via combined X-ray diffraction (XRD), transmission electron microscopy (TEM), selected area electron diffraction (SAED), aberration-corrected high-angle annular dark field scanning transmission electron microscopy (HAADF-STEM), and energy dispersive X-ray (EDX) elemental mapping. As can be seen in Figure S1 (Supporting Information), no diffraction peaks from metallic crystals in XRD patterns (cubic CdS, JCPDS #10-0454) were detected, evidencing the absence of Co or Au particles. The as-synthesized CdS NPs exhibited a mean size of 19.7 nm (Figure S2a,b, Supporting Information). The HAADF-STEM image (Figure S2c, Supporting Information) evidenced a lattice distance of 0.34 nm, assigned to the (111) facet of cubic CdS. Following loading Au/Co

DSAs on CdS NPs, the morphology and crystal structure were established. From **Figure 1**a,b, it is seen that CAC2 exhibits the same morphology and crystal structure as that for CdS NPs (Figure S2, Supporting Information). However, SAs were evidenced on CAC2 using atomic-resolution HAADF-STEM- these are highlighted by yellow-color circles (Figure 1c). These are attributed to Au SAs (Figure S3, Supporting Information), because the atomic number for Cd of $z = 48$ is greater than that for Co of $z = 27$, however lower than that for Au ($z = 79$). Figure 1c evidences lattice spacing of 0.21 nm, attributed to the (220) facet of cubic CdS. The HAADF-STEM and corresponding EDX elemental mapping images of CAC2, Figure 1d, confirm the homogenous loading of Au and Co on CdS NPs. CA2 and CC2 were assessed via XRD (Figure S1, Supporting Information) and HAADF-STEM with EDX elemental mapping (Figures S4 and S5, Supporting Information) with findings evidencing homogeneous loading of Au and Co SA on CdS NPs for CA2 and CC2, respectively. Raman spectra (Figure S6, Supporting Information) evidenced the existence of Co—S bond at ≈ 660 cm^{-1} for both CC2 and CAC2.[45–47] Additionally, the existence of Au—S bond at ≈ 400 cm^{-1} was evidenced for both CA2 and CAC2.[45–47] It was concluded therefore that findings confirmed the successful loading of Au/Co DSAs for CAC2, Au SA for CA2, and Co SA for CC2.

To establish the valence state and coordination environment of Au or Co SA, synchrotron-based X-ray absorption near edge structure (XANES) and extended X-ray absorption fine structure (EXAFS) of CAC2, CA2, and CC2 were determined. The XANES spectra for Au L_3-edge, **Figure 2**a, evidenced the higher oxidation state for Au in CA2 or CAC2 (Au$^{\delta+}$, $\delta > 0$), compared with that for Au-foil. The EXAFS spectra for Au-foil, Figure 2b, exhibited two peaks at ≈ 2.5 and ≈ 2.9 Å, which were attributed to typical Au—Au scattering. EXAFS spectra for both CA2 and CAC2, Figure 2b, exhibit a prominent peak at ≈ 1.8 Å, which is assigned to the Au—S bonds and with the absence of Au—Au bonds. This finding confirms the successful loading of SA Au in both CA2 and CAC2. Significantly, the XANES spectra of Co K edge (Figure 2c) evidence the higher oxidation states of Co in CC2 or CAC2, compared with that for Co-foil. The EXAFS spectra for Co-foil (Figure 2d) exhibit one peak at ≈ 2.2 Å, which is attributed to Co—Co scattering. The absence of Co—Co scattering and the existence of characteristic peak assigned to Co—S contribution at ≈ 1.8 Å (Figure 2d) evidence the SA status of Co in both CC2 and CAC2. The fitted EXAFS (Figure S7 and Table S1, Supporting Information) demonstrate that the Au—S and Co—S are ≈ 2 and 4 coordinated, respectively. It is concluded these findings confirm the SA status and the coordination of Au and Co on CdS NPs.

To reinforce coordination data, wavelet transform analysis of the k^3-weighted EXAFS spectra for CAC2, CA2, CC2, and reference metal foils were determined, Figure 2e–h (and Figure S8, Supporting Information). The maximum intensity for Au L_3-edge spectra of CA2 and CAC2 in Figure 2e,f is at 8.5 Å^{-1} that is attributed to Au—S configuration. The maximum intensity for Co K-edge spectra in Figure 2g,h is at 5 Å^{-1} for CC2 or CAC2, corresponding to Co—S configuration. In contrast the maximum intensity for Au L_3-edge and Co K-edge spectra in Figure S8a (Supporting Information) (Au-foil) and b (Co-foil) are located at 10 and 7.5 Å^{-1}, respectively, and are attributed to Co—Co and Au—Au configuration. These findings were concluded to confirm the

**ADVANCED
SCIENCE NEWS**
www.advancedsciencenews.com
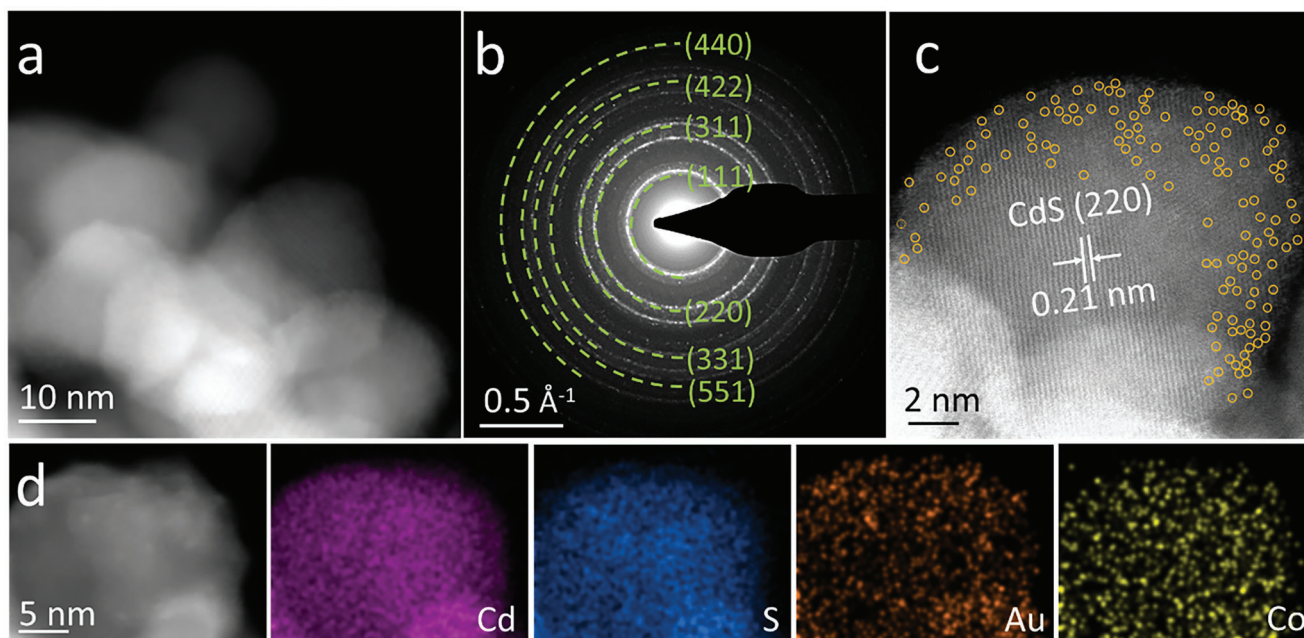
**ADVANCED
MATERIALS**
www.advmat.de

Figure 1. a) TEM image and b) Corresponding selected area electron diffraction (SAED) pattern for CAC2. c) Atomic-resolution HAADF-STEM image of CAC2. d) HAADF-STEM image and corresponding EDS elemental mapping of CAC2.
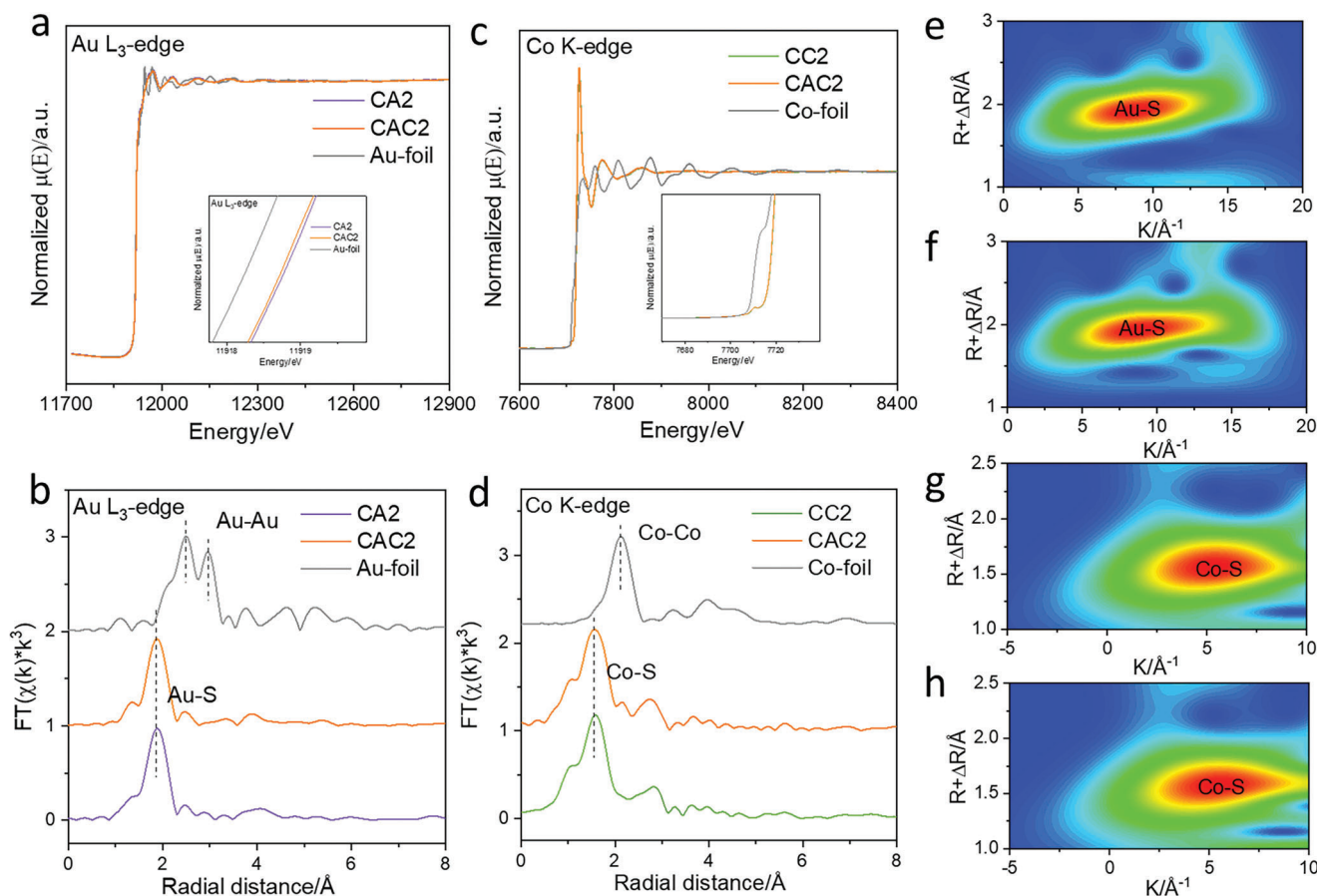

Figure 2. a) XANES and b) Corresponding EXAFS spectra for Au L$_3$-edge for CAC2, CA2, and Au-foil. c) XANES and d) Corresponding EXAFS spectra for Co K-edge for CAC2, CC2, and Co-foil. WT analysis for the k^3-weighted EXAFS spectra at Au L$_3$-edge for e) CA2 and f) CAC2. WT analysis for the k^3-weighted EXAFS spectra at Co K-edge for g) CAC2 and h) CC2.
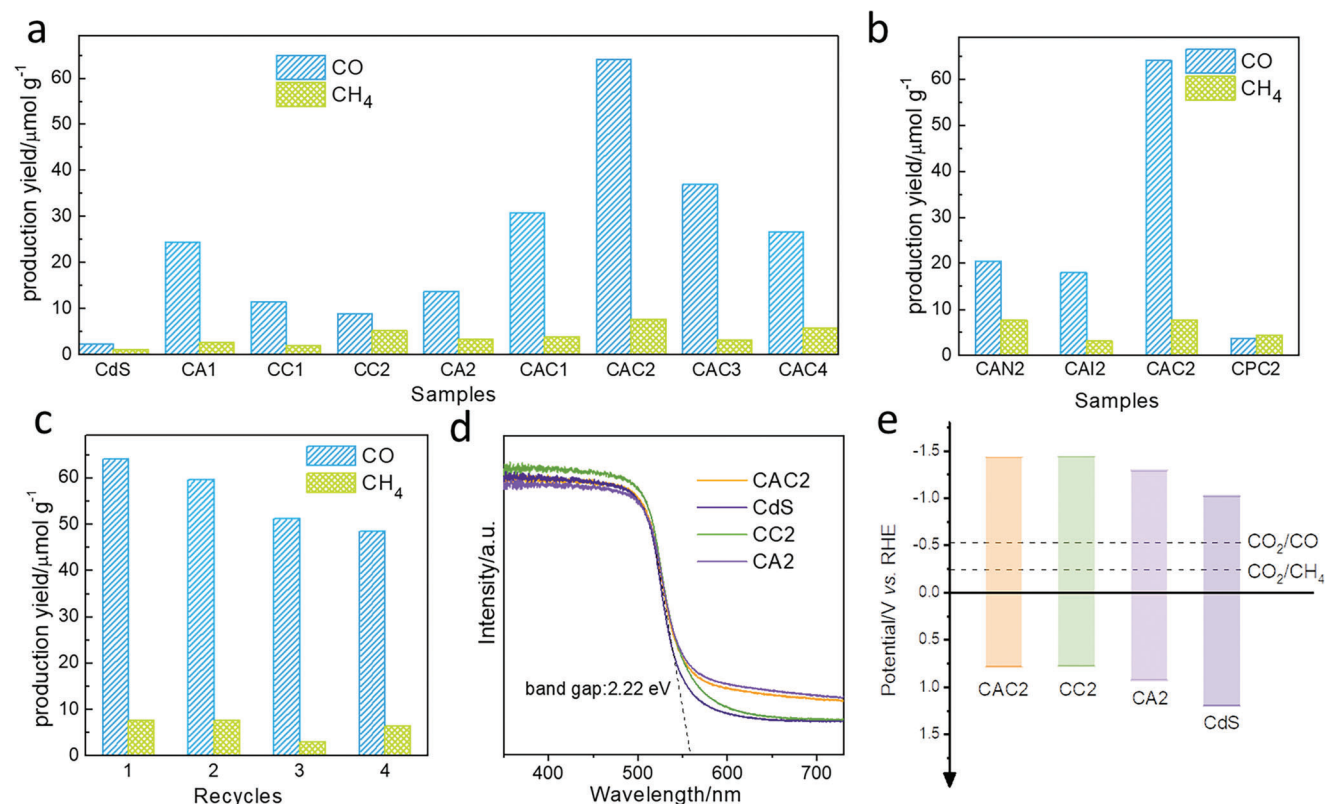
2306923 (3 of 9)

ADVANCED
SCIENCE NEWS

www.advancedsciencenews.com

ADVANCED
MATERIALS

www.advmat.de

Figure 3. a) Photocatalytic CO_2 reduction for, CdS, CA1, CC1, CC2, CA2, CAC1, CAC2, CAC3, and CAC4 under visible-light illumination ($\lambda > 400$ nm). b) Photocatalytic CO_2 reduction for CAN2, CAI2, CAC2, and CPC2 under visible-light illumination ($\lambda > 400$ nm). c) Stability test for CAC2 under visible-light illumination ($\lambda > 400$ nm). Each test was for 7 h. d) UV–vis spectra for CdS, CA2, CC2, and CAC2. e) Schematic for band structures for CdS, CA2, CC2, and CAC2.

absence of Co—Co or/and Au—Au bond in CA2, CC2, and CAC2. This corroborates the SA nature of Co or/and Au in CA2, CC2, and CAC2. For CAC2, no Au—Co configuration is evidenced in Figure 2b,d,f,g, confirming the absence of Co—Au alloy in CAC2, and evidencing that Co and Au are atomically dispersed in CAC2.

To visualize the different configuration/loading for DSA for CO_2 photoreduction activity findings are presented in **Figure 3**a. It is seen in the figure that CdS exhibits limited CO_2 photoreduction yields for CO of 2.3 µmol g^{-1} and CH_4 of 1.12 µmol g^{-1}. SA Au loaded CdS NPs, however boosts CO_2 photoreduction for both CA1, namely, CO: 24.3 µmol g^{-1} and CH_4: 2.6 µmol g^{-1}, and CA2, CO: 13.7 µmol g^{-1} and CH_4 3.3 µmol g^{-1}. Compared with CA1, CA2 exhibits reduced CO yield, however an increased CH_4 yield, Figure 3a. A similar trend was found for SA Co-loaded CdS NPs (CC1 and CC2). As is seen in Figure 3a, compared with those for CdS alone, increased CO_2 photoreduction is apparent for both CC1 (CO: 11.4 µmol g^{-1} and CH_4: 1.9 µmol g^{-1}) and CC2 (CO: 8.8 µmol g^{-1} and CH_4: 5.1 µmol g^{-1}). Compared with CC1, CC2 exhibits a decreased CO yield and an increased CH_4 yield, Figure 3a. It is concluded therefore that loading SA Au or Co on CdS NPs significantly increases yield for CO and CH_4. The greater loading for SA Au (CA2) or Co (CC2) leads to the greater higher of 8-electrons/protons involved reaction product, CH_4. These findings might arise from the available electrons accumulated around SA Au in CA2 or SA Co in CC2, compared with that in CA1 or CC1. CC2 exhibited the greatest CH_4 yield of

5.1 µmol g^{-1}, evidencing that SA Co is more favorable for CH_4 generation compared with SA Au. Au/Co DSA-loaded CdS NPs (CAC1, CAC2, CAC3, and CAC4) were assessed for CO_2 photoreduction. The four samples exhibited the same loading of SA Au, except that the loading for SA Co was gradually increased from CAC1 to CAC4. CAC2 exhibited the greatest CO_2 photoreduction yields, CO: 64.1 µmol g^{-1} and CH_4: 7.7 µmol g^{-1}, as is seen in Figure 3a. Compared with CAC2, further increasing SA Co content in CAC3 and CAC4 resulted in reduced yields for both CO and CH_4, Figure 3a. It is hypothesized that these findings arise because of a "shielding effect" via excessive loading of SA Co. The actual metal site concentration of Table S2 (Supporting Information) demonstrates that CAC2 is not the greatest loading metal sample, importantly, evidencing the boosted performance does not originate from increasing loaded metal sites.

To determine the role of Au/Co DSAs in CO_2 photoreduction, a series of DSA-loaded CdS NPs were synthesized including, Au/Ni DSA (CAN2), Au/In DSA (CAI2) and Pt/Co DSA (CPC2), and tested. Detailed preparation and testing are included in Supporting Information. As presented in Figure 3b, CAC2 exhibits the greatest CO yield of 9.2 µmol g^{-1} and the second-highest CH_4 yield of 1.1 µmol g^{-1}. It is concluded that these findings confirm the unique and strong synergistic effect in Au/Co DSA for CO_2 photoreduction CPC2 exhibited significantly low CO_2 photoreduction yields for, CO: 3.6 µmol g^{-1} and CH_4: 4.4 µmol g^{-1}. This is attributed to the strong absorption of CO on Pt that, is

**ADVANCED
SCIENCE NEWS**

www.advancedsciencenews.com

**ADVANCED
MATERIALS**

www.advmat.de

not favorable for the generation of CO or CH_4.[48] Stability and reproducibility for CAC2 were established. Following four-time recycles (28 h), CO and CH_4 yields were ≈80% of the first cycle, Figure 3c. Compared with independently reported values, Table S3 (Supporting Information), CAC2 exhibited excellent CO_2 photoreduction under similar conditions, confirming the superiority of DSA materials. XRD, XPS, and TEM and electron diffraction (Figures S9–13, Supporting Information) findings following performance testing evidenced no apparent changes, confirming high stability of the crystal structures and loaded metal sites. To determine the effect of possible carbon impurities, blank experiments with negligible products were conducted in ultrahigh purity argon rather than CO_2. Findings confirmed the negligible influence of carbon impurities (Figure S14, Supporting Information) and that CO and CH_4 were generated from photocatalytic CO_2 reduction.

To establish the origin of boosted activity and reaction mechanism, a range of state-of-the-art characterizations and theoretical computations were conducted. As is seen in Figure 3d, the absorption edges of the samples are located at 558 nm, evidencing the same band gap width of 2.22 eV. Compared with CdS, CA2, CC2, and CAC2 exhibited boosted light absorption in the range ≈560 to 800 nm. To determine the effect of this boosted light absorption, CO_2 photoreduction was conducted under the same reaction conditions, except for the substitution of visible light with a 630 nm light-emitting diode (LED) light. Low yields were exhibited in all samples (Figure S15, Supporting Information), evidencing limited contribution of boosted light absorption to activity. To establish electronic band structures XPS valence band (VB) spectra (Figure S16, Supporting Information) and Mott-Schottky plots were determined (Figure S17, Supporting Information). As can be seen in Figure S16 (Supporting Information), the XPS VB edges of CdS, CA2, CC2, and CAC2 are at 1.5, 1.3, 1.2, and 1.2 eV, respectively. The Mott–Schottky plots (Figure S17, Supporting Information) evidenced that the flat band potentials for CdS, CA2, CC2, and CAC2 are at, respectively, −0.90, −0.97, −1.02 and −1.01 V versus Ag/AgCl electrode. The Fermi levels for CdS, CA2, CC2, and CAC2 were estimated to be at, −0.30, −0.37, −0.42, and −0.41 V versus reversible hydrogen electrode (RHE). The actual VB edges of CdS, CA2, CC2, and CAC2 are at 1.20, 0.93, 0.78, and 0.79 V versus RHE. Therefore the conduction band (CB) edges of CdS, CA2, CC2, and CAC2 are at −1.02, −1.29, −1.44, and −1.43 V versus RHE. As is seen in Figure 3e, compared with the CB edge of CdS, the CB edges of CA2, CC2, and CAC2 exhibit upshift, evidencing greater reduction ability of photo-generated electrons for CO_2 photoreduction.

To determine the photo-generated charge dissociation/transfer, transient-state photoluminescence (TSPL) spectroscopy, transient photocurrent (TPC) density measurement, and electrochemical impedance spectroscopy (EIS) were conducted. As can be seen in Figure S18 and Table S4 (Supporting Information), the "averaged charge lifetimes" (τ_{ave}) are shortened for CA2 (τ_{ave} = 3.18 ns), CC2, (τ_{ave} = 3.37 ns) and CAC2 (τ_{ave} = 2.73 ns), in contrast to that for CdS (τ_{ave} = 3.87 ns). It is concluded that these findings confirm that loading SA Au and/or SA Co significantly promotes charge transfer.[8] The τ_{ave} ranking is, CdS > CC2 > CA2 > CAC2, and is in reverse with photocatalytic CO yield, namely, CAC2 > CA2 > CC2 > CdS; Figure 3a. Significantly, these findings evidence a strong synergistic effect

of loading Au/Co DSA in boosting charge migration that is confirmed via TPC density measurement (Figure S19, Supporting Information) and EIS spectra (Figure S20, Supporting Information). CAC2 exhibited the greatest TPC density among samples, evidencing the greatest charge separation efficiency via loading Au/Co DSA (Figure S19, Supporting Information). CAC2 exhibited the least charge transfer resistance of R_{ct} = 197 Ω, compared with CdS of R_{ct} = 4300 Ω, CA2 (R_{ct} = 2600 Ω), and CC2 (R_{ct} = 3050 Ω), as can be seen in Figure S20 (Supporting Information). It can be concluded therefore TSPL, TPC and EIS findings confirm the greatest charge separation/migration efficiency in CAC2 by Au/Co DSA deposition.

To determine how the Au/Co DSA boosts charge separation/transfer in CAC2, combined in situ characterizations and theoretical computation were conducted. CA2, CC2, and CAC2 were characterized via in situ XPS. As is seen in **Figure 4**a, with light-on, the Au 4f peaks for CA2 exhibit a left-shift of 0.7 eV to the lower binding energy direction, compared with those with light-off. This finding evidences the transfer of photo-generated electrons from CdS to SA Au in CA2 with light illumination. Similarly, Figure 4b evidences the migration of photo-generated electrons from CdS to SA Co in CC2 with light-on. With light-on, the Au 4f peaks for CAC2 exhibit a right-shift of 0.2 eV to higher binding energy direction, Figure 4c, while the Co 2p peaks for CAC2 exhibit a left-shift of 0.4 eV to lower binding energy direction, Figure 4d. The shift of these peaks evidences that the surface electrons are localized around different areas that were positively or negatively charged.

These findings evidence the transfer of photo-generated electrons to SA Co, while the holes to Au in CAC2 separately. Therefore with light illumination, photo-generated electrons are localized around SA Co and delocalized from SA Au on CAC2. Density functional theory (DFT) based theoretical computation simulated electron redistribution and mechanism. As seen in Figure 4e, with additional electrons in the Au/Co DSA loaded CdS, there is formed an electron accumulation area around SA Co while an electron depletion area is formed around Au SA, as evidenced via charge density difference.[48,49] The localized electrons around SA Co were analyzed via Bader charge. It can be seen from Figure S21 (Supporting Information) that more electrons are localized around Co in Au/Co DSA-loaded CdS (CAC-Co) compared with that in SA Co-loaded CdS (CC-Co). This finding confirms promoted electron redistribution via loading Au/Co DSA. The integrated partial density of states (PDOS) of uncaptured electrons above the Fermi level in SA Co loaded CdS model (CC), SA Au loaded CdS model (CA) and Au/Co DSA loaded CdS model (CAC) are presented in Figure S22 and Table S5 (Supporting Information). More uncaptured electrons evidence a more electron-deficiency of atoms, confirming weaker ability to capture electrons.[41,50] As can be seen in Table S5 (Supporting Information), CAC exhibits less uncaptured electrons in Co (1.2) compared with CC (1.8), however, more uncaptured electrons in Au (1.1) compared with CA (0.4). Co in CAC therefore exhibits greater ability to capture electrons compared with Co in CC; Au in CAC exhibits lesser ability to capture electrons compared with Au in CA. To establish internal factors affecting electron redistribution, the potential profiles for CA, CC, and CAC models were computed. Findings evidenced that photogenerated charges can be redistributed between Co and Au SAs on the CdS
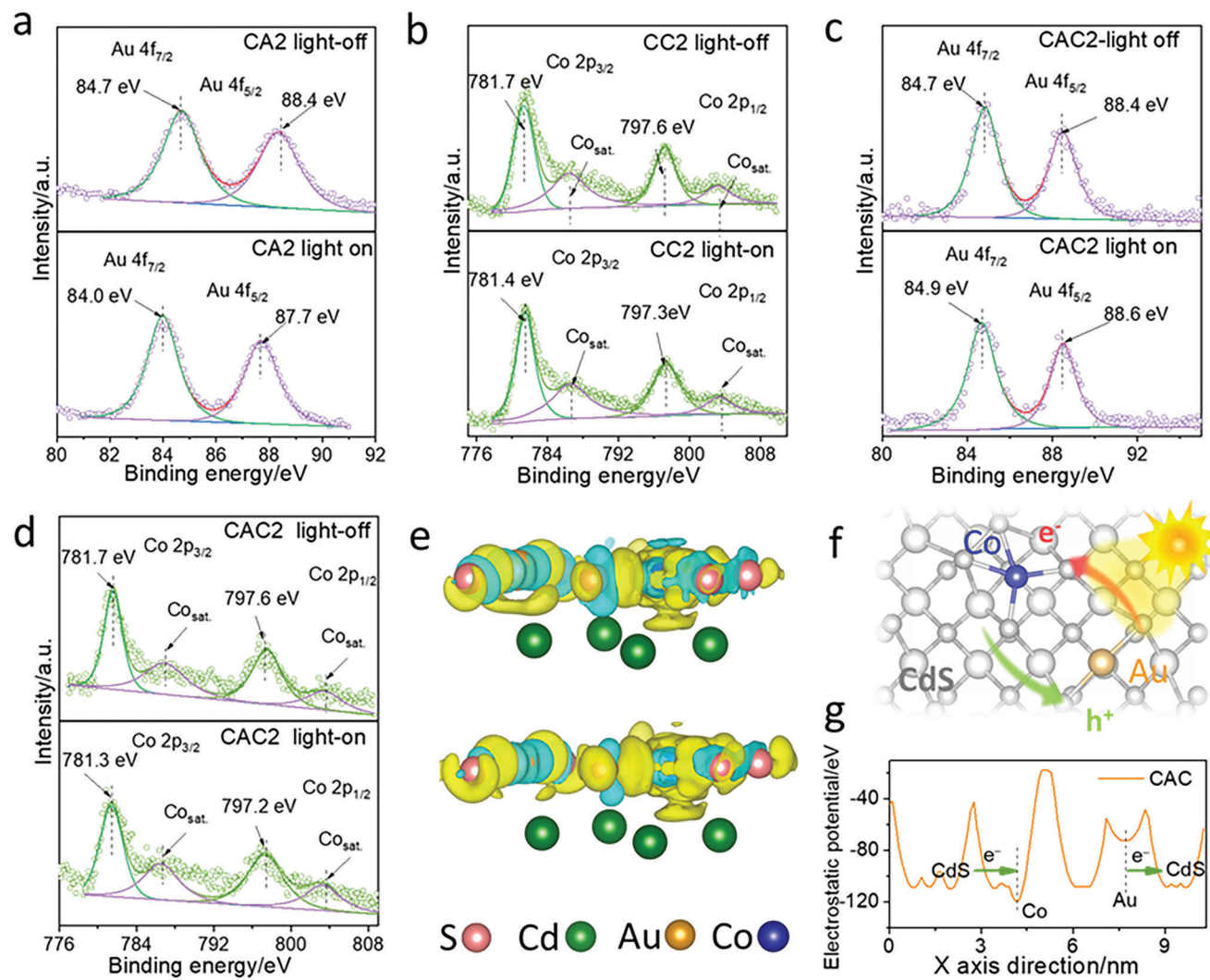
Figure 4. a) High-resolution XPS spectra for Au 4f for CA2 with light-on and -off, respectively. b) High-resolution XPS spectra for Co 2p for CC2 with light-on and -off, respectively. c) High-resolution XPS spectra for Au 4f for CAC2 with light-on and -off, respectively. d) High-resolution XPS spectra for Co 2p for CAC2 with light-on and -off, respectively. e) Charge density distribution of CAC before (top side) and following (bottom side) introduction of extra electrons in the model. The iso-surface value is 0.0045e Å^{-3}. Charge depletion and accumulation are labeled in cyan-color and yellow, respectively. f) Scheme for charge redistribution between DSA and CdS nanoparticles under illumination. g) Electrostatic potential energy along the x-axis for CAC model.

nanoparticles under illumination, Figure 4f. As is seen in Figure 4g and Figure S23 (Supporting Information), along the x-axis of CAC model, the potential energy of CdS is greater than that for Co, however it is lesser than that for Au. The electrostatic driving force therefore boosts electron transfer from Au to CdS and CdS to Co, resulting in different electron localizations. In contrast, for CA or CC models, Au or Co exhibits a lower potential energy than for CdS (Figures S24 and S25, Supporting Information), resulting in the driving force from CdS to SA Au or Co. This results in electron localization around SA Au or Co. The in situ XPS findings, together with computations therefore confirm electron localization around SA Co/Au. However, electron delocalization around Au and localization around Co in CAC leads to the promoted charge redistribution in CAC2.

The adsorption, activation, and reduction of CO_2 were determined via combining advanced characterizations and DFT com-

putation. Because the adsorption of CO_2 on the catalyst surface is necessary as a prerequisite for CO_2 conversion, the behavior of CO_2 adsorption on catalysts using CO_2 temperature programmed desorption (TPD) and in situ diffuse reflectance infrared Fourier transform spectroscopy (DRIFTS) we established. As is seen in **Figure 5a**, the desorption of absorbed *CO_2 can conveniently be categorized into three temperature regions, 50–180, 180–350, and >350 °C that correspond to, respectively, weak, moderate, and strong CO_2 adsorption active sites. No apparent CO_2 desorption signal was exhibited for CdS, Figure 5a, evidencing the absence of CO_2 adsorption sites on bare CdS. In contrast, CA2 or CC2 exhibited significantly stronger CO_2 desorption signals in the region >350 °C, Figure 5a, evidencing that the loaded SA Au or Co is the strong active site that absorbs CO_2 molecules. Significantly, CAC2 exhibited the strongest CO_2 desorption signals in the region >350 °C, Figure 5a, demonstrating the

2306923 (6 of 9)

ADVANCED
SCIENCE NEWS
www.advancedsciencenews.com
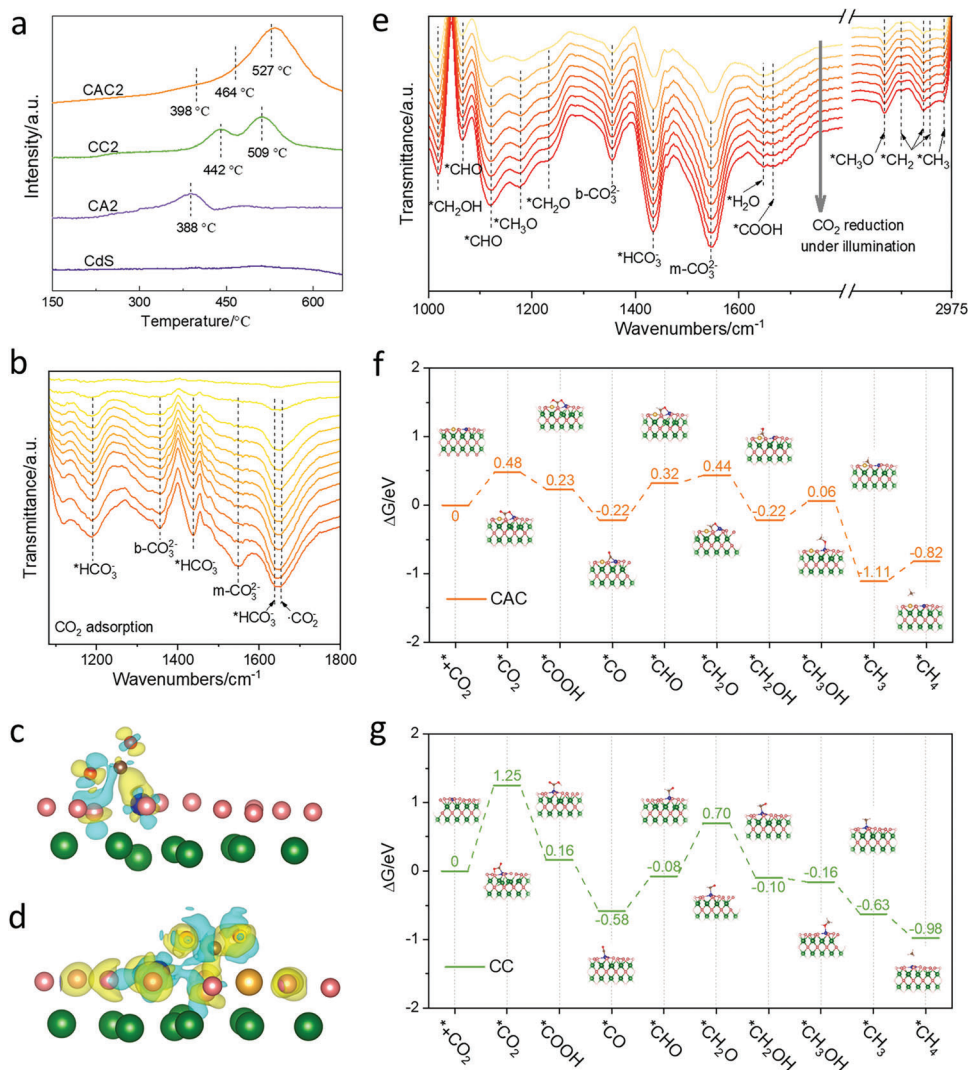
ADVANCED
MATERIALS
www.advmat.de

Figure 5. a) CO_2 TPD findings for CdS, CC2, CA2, and CAC2. b) in situ DRIFTS spectra for CO_2 adsorption on CAC2 in darkness from 0 to 40 min. The charge difference distributions for c) CC and d) CAC following CO_2 adsorption. The iso-surfaces are 0.003 e $Å^{-3}$. Charge depletion and accumulation are labeled in, respectively, cyan-color and yellow. Cd, S, O, C, Co, and Au are shown as green-color, pink, red, brown, blue, and yellow, balls, respectively. e) In situ DRIFTS spectra for CO_2 photoreduction for CAC2 from 0 to 40 min under illumination. Computed Gibbs free energy and corresponding configuration for steps in photocatalytic CO_2-to-CH_4 conversion on f) CAC and g) CC.

synergistic effect of loading Au/Co DSA as strong active sites for CO_2 adsorption. To establish the chemisorbed species on catalysts, in situ DRIFTS spectra were determined in CO_2 atmosphere and darkness. The data of Figure 5b confirm several intermediates for CO_2 chemisorption including typical intermediates for generating products. As is seen in Figure 5b, the peaks at 1355 and 1547 cm^{-1} can be attributed to bidentate carbonate (b-CO_3^{2-}) and monodentate carbonates (m-CO_3^{2-}), respectively.[51] The formation of HCO_3^- via coadsorption of H_2O and CO_2 is evidenced via the peaks at 1637, 1438, and 1190 cm^{-1} (Figure 5b).[52,53] The rising peak at 1650 cm^{-1} with increasing time is from the vibration of $\cdot CO_2^-$, an important indicator for the yield of CH_4.[9] The strong signals for chemisorbed species on CAC2 (Figure 5b) evidence the high concentration of chemisorbed species, because of the high affinity of Au/Co DSA for CO_2 molecules. This ability of CAC2 is important

to CO_2 photoreduction. In contrast, CdS exhibits significantly weaker signals in the same condition (Figure S26a, Supporting Information) because of significantly less adsorbed surface moieties. Compared with CAC2, CA2 exhibited similar signals for chemisorbed species, however with reduced intensity, especially for the signal for b-CO_3^{2-} (Figure S27a, Supporting Information). Significantly, the signal for m-CO_3^{2-} was significantly reduced for CC2 in the same conditions (Figure S28a, Supporting Information). It is concluded therefore that findings confirm the strongest CO_2 adsorption ability of CAC2 via loading Au/Co DSA. The surface oxidation reaction in water vapor provides protons for CO_2 reduction. Importantly, the in situ DRIFTS findings are consistent with the CO_2 TPD findings (Figure 5a). To establish CO_2 chemisorption on CAC2, DFT computation was used. As shown in Figure 5c,d, more electrons are transferred from CAC to CO_2 compared with those from CC to

2306923 (7 of 9)

ADVANCED
SCIENCE NEWS

www.advancedsciencenews.com

**ADVANCED
MATERIALS**

www.advmat.de

CO_2, confirming CO_2 adsorption/activation by Au/Co DSA in CAC2.

To establish a mechanistic understanding of photocatalytic CO_2 reduction with the DSAs, in situ DRIFTS spectra were determined in CO_2 atmosphere and under light illumination. With light illumination as an indicator for CO_2 to CO conversion, *COOH at 1667 cm^{-1} was detected on CAC2, Figure 5e. This is an important intermediate. Fast conversion of COOH leads to weak signals in the spectrum. As is seen in Figure 5e, the signals for carbonate species, *HCO_3^-, b-CO_3^{2-} and m-CO_3^{2-}, are significantly increased with increasing illumination time, confirming that CO_2 is more readily activated with light illumination to supply increased intermediates for conversion on CAC2. Additionally, some new bands, e.g., *CHO, *CH_2O, *CH_3O, and *CH_3, were observed for CAC2, Figure 5e, which are important intermediates for CH_4 generation.[9,50] The signals for in situ DRIFTS spectra for CdS (Figure S26b, Supporting Information), CA2, (Figure S27b, Supporting Information), and CC2 (Figure S28b, Supporting Information) are, in contrast, significantly weaker, confirming the strongest CO_2 adsorption/activation/reduction ability of CAC2 with light illumination. Based on these, and in situ DRIFTS findings for CAC2, a reaction pathway is hypothesized, namely: *CO_2 → HCO_3^-/CO_3^{2-} → *COOH → *CO → *CHO → *CH_2O → *CH_3OH → *CH_3 → *CH_4. This pathway was simulated via DFT computation of the corresponding free energy change (ΔG) for each reaction step, Figure 5f,g, on CAC and CC. As can be seen in Figure S29 (Supporting Information), the overall energy barriers for CAC are less than those for CC, confirming that Au/Co DSA boosts CO_2 photoreduction. The rate-limiting step for CO_2 to CH_4 conversion on CAC or CC is chemisorption of CO_2 molecules. In CO_2 chemisorption, CC exhibits a highly significant energy barrier of 1.25 eV, Figure 5g, while CAC exhibits a significantly lower energy barrier of 0.48 eV (Figure 5f). This finding evidences boosted CO_2 adsorption by Au/Co DSA and is confirmed via the surface charge distribution following CO_2 adsorption on CC and CAC (Figure 5c,d). More electron transfer occurs between CAC and CO_2, Figure 5d, compared with that between CC and CO_2 (Figure 5c) because of the ready adsorption/activation of CO_2 by Au/Co DSA. CO_2 chemisorption is however more difficult on CA or CdS. As can be seen in Figure S30 (Supporting Information), trace electron transfer between CO_2 and CdS or CA is apparent. The bond angle (180°) and bond length (1.17 Å) for absorbed CO_2 molecules are not changed, confirming the significantly weaker CO_2 chemisorption on CA or CdS compared with that on CAC, Figure 5d, or CC, Figure 5c. Importantly, these findings accord with the CO_2 TPD findings (Figure 5a). Significantly, the greatest energy barrier of 0.54 eV is exhibited for the step, *CO hydrogenation on CAC, Figure 5f, confirming that CO is the major product on CAC.

3. Conclusion

The reversal of electron transfer direction was confirmed when loading Au and Co SA concurrently. Combined state-of-art characterizations and theoretical computation evidenced that the localized electrons around Co and delocalized electrons from Au in DSA catalysts create a polarized region boosting the reduction of CO_2. This reversed electron transfer direction in Au/Co DSA

arises from different electrostatic potentials among Au, Co, and CdS. Consequently, respectively, ≈2800% and 700% greater generation of CO and CH_4 was exhibited on Au/Co DSA loaded Cd. Importantly, Au/Co DSA-loaded CdS exhibited a robust stability of >28 h. Findings aid explanation of photogenerated electron transfer on catalysts at the atomic level and, electron migration mechanism in DSA for design of atomic-level catalysts for solar energy conversion. These will benefit the development of DSA-loaded catalysts for the generation of solar fuels.

Conflict of Interest

The authors declare no conflict of interest.

Data Availability Statement

The data that support the findings of this study are available from the corresponding author upon reasonable request.

[1] Y. Zhang, B. Xia, J. Ran, K. Davey, S.-Z. Qiao, *Adv. Energy Mater.* **2020**, *10*, 1903879.
[2] J. Albero, Y. Peng, H. GarcC-a, *ACS Catal.* **2020**, *10*, 5734.
[3] J. Fu, K. Jiang, X. Qiu, J. Yu, M. Liu, *Mater. Today* **2020**, *32*, 222.
[4] Y. Zhang, D. Yao, B. Xia, M. Jaroniec, J. Ran, S.-Z. Qiao, *ACS Energy Lett.* **2022**, *7*, 1611.
[5] S. Ji, Y. Qu, T. Wang, Y. Chen, G. Wang, X. Li, J. Dong, Q. Chen, W. Zhang, Z. Zhang, S. Liang, R. Yu, Y. Wang, D. Wang, Y. Li, *Angew. Chem., Int. Ed.* **2020**, *59*, 10651.

[6] S. Zhu, X. Li, X. Jiao, W. Shao, L. Li, X. Zu, J. Hu, J. Zhu, W. Yan, C. Wang, Y. Sun, Y. Xie, *Nano Lett.* **2021**, *21*, 2324.

[7] Y. Zhang, X. Zhi, J. Harmer, H. Xu, K. Davey, J. Ran, S.-Z. Qiao, *Angew. Chem., Int. Ed.* **2022**, *61*, e202212355.

[8] Y. Cao, L. Guo, M. Dan, D. E. Doronkin, C. Han, Z. Rao, Y. Liu, J. Meng, Z. Huang, K. Zheng, P. Chen, F. Dong, Y. Zhou, *Nat. Commun.* **2021**, *12*, 1675.

[9] J. Sheng, Y. He, M. Huang, C. Yuan, S. Wang, F. Dong, *ACS Catal.* **2022**, *12*, 2915.

[10] Y. Zhang, D. Yao, B. Xia, H. Xu, Y. Tang, K. Davey, J. Ran, S.-Z. Qiao, *Small Sci.* **2021**, *1*, 2000052.

[11] Y. Zhang, X. Wang, P. Dong, Z. Huang, X. Nie, X. Zhang, *Green Chem.* **2018**, *20*, 2084.

[12] H. Yu, F. Chen, X. Li, H. Huang, Q. Zhang, S. Su, K. Wang, E. Mao, B. Mei, G. Mul, T. Ma, Y. Zhang, *Nat. Commun.* **2021**, *12*, 4594.

[13] J. Di, C. Zhu, M. Ji, M. Duan, R. Long, C. Yan, K. Gu, J. Xiong, Y. She, J. Xia, H. Li, Z. Liu, *Angew. Chem., Int. Ed.* **2018**, *57*, 14847.

[14] L. Hao, H. Huang, Y. Zhang, T. Ma, *Adv. Funct. Mater.* **2021**, *31*, 2100919.

[15] Y. He, H. Rao, K. Song, J. Li, Y. Yu, Y. Lou, C. Li, Y. Han, Z. Shi, S. Feng, *Adv. Funct. Mater.* **2019**, *29*, 1905153.

[16] J. Di, X. Zhao, C. Lian, M. Ji, J. Xia, J. Xiong, W. Zhou, X. Cao, Y. She, H. Liu, K. P. Loh, S. J. Pennycook, H. Li, Z. Liu, *Nano Energy* **2019**, *61*, 54.

[17] L. Liu, S. Wang, H. Huang, Y. Zhang, T. Ma, *Nano Energy* **2020**, *75*, 104959.

[18] K. M. Cho, K. H. Kim, K. Park, C. Kim, S. Kim, A. Al-Saggaf, I. Gereige, H.-T. Jung, *ACS Catal.* **2017**, *7*, 7064.

[19] Y. Zhang, X. Wang, P. Dong, Z. Huang, X. Nie, X. Zhang, *RSC Adv.* **2018**, *8*, 15991.

[20] X. Xiong, C. Mao, Z. Yang, Q. Zhang, G. I. N. Waterhouse, L. Gu, T. Zhang, *Adv. Energy Mater.* **2020**, *10*, 2002928.

[21] X.-Y. Dong, Y.-N. Si, Q.-Y. Wang, S. Wang, S.-Q. Zang, *Adv. Mater.* **2021**, *33*, 2101568.

[22] Y. Yu, X. Dong, P. Chen, Q. Geng, H. Wang, J. Li, Y. Zhou, F. Dong, *ACS Nano* **2021**, *15*, 14453.

[23] H. Shi, H. Wang, Y. Zhou, J. Li, P. Zhai, X. Li, G. G. Gurzadyan, J. Hou, H. Yang, X. Guo, *Angew. Chem., Int. Ed.* **2022**, *61*, e202208904.

[24] Y. Li, B. Li, D. Zhang, L. Cheng, Q. Xiang, *ACS Nano* **2020**, *14*, 10552.

[25] G. Jia, M. Sun, Y. Wang, Y. Shi, L. Zhang, X. Cui, B. Huang, J. C. Yu, *Adv. Funct. Mater.* **2022**, *32*, 2206817.

[26] Z. Luo, X. Ye, S. Zhang, S. Xue, C. Yang, Y. Hou, W. Xing, R. Yu, J. Sun, Z. Yu, X. Wang, *Nat. Commun.* **2022**, *13*, 2230.

[27] B. Xia, B. He, J. Zhang, L. Li, Y. Zhang, J. Yu, J. Ran, S.-Z. Qiao, *Adv. Energy Mater.* **2022**, *12*, 2201449.

[28] L. Zhang, H. H. Mohamed, R. Dillert, D. Bahnemann, *J Photochem Photobiol* **2012**, *13*, 263.

[29] J. C. Zhang, H. B. Yang, B. Liu, *Adv. Energy Mater.* **2021**, *11*, 2002473.

[30] J. Zhang, W. Cai, F. X. Hu, H. Yang, B. Liu, *Chem. Sci.* **2021**, *12*, 68.

[31] J. Yang, W. Li, D. Wang, Y. Li, *Small Struct.* **2021**, *2*, 2000051.

[32] R. Li, D. Wang, *Nano Res.* **2022**, *15*, 6888.

[33] Y. Liu, W. Yang, Q. Chen, D. A. Cullen, Z. Xie, T. Lian, *J. Am. Chem. Soc.* **2022**, *144*, 2705.

[34] H. Peng, T. Yang, H. Lin, Y. Xu, Z. Wang, Q. Zhang, S. Liu, H. Geng, L. Gu, C. Wang, X. Fan, W. Chen, X. Huang, *Adv. Energy Mater.* **2022**, *12*, 2201688.

[35] J. Zhang, H. Yang, J. Gao, S. Xi, W. Cai, J. Zhang, P. Cui, B. Liu, *Carbon Energy* **2020**, *2*, 276.

[36] L. Zhang, R. Long, Y. Zhang, D. Duan, Y. Xiong, Y. Zhang, Y. Bi, *Angew. Chem., Int. Ed.* **2020**, *59*, 6224.

[37] P. Zhou, H. Chen, Y. Chao, Q. Zhang, W. Zhang, F. Lv, L. Gu, Q. Zhao, N. Wang, J. Wang, S. Guo, *Nat. Commun.* **2021**, *12*, 4412.

[38] C. Wang, K. Wang, Y. B. Feng, C. Li, X. Y. Zhou, L. Y. Gan, Y. J. Feng, H. J. Zhou, B. Zhang, X. L. Qu, H. Li, J. Y. Li, A. Li, Y. Y. Sun, S. B. Zhang, G. Yang, Y. Guo, S. Z. Yang, T. H. Zhou, F. Dong, K. Zheng, L. H. Wang, J. Huang, Z. Zhang, X. D. Han, *Adv. Mater.* **2021**, *33*, 2003327.

[39] L. Cheng, X. Yue, L. Wang, D. Zhang, P. Zhang, J. Fan, Q. Xiang, *Adv. Mater.* **2021**, *33*, 2105135.

[40] X. Zhao, F. Wang, X.-P. Kong, R. Fang, Y. Li, *J. Am. Chem. Soc.* **2021**, *143*, 16068.

[41] D. Yao, C. Tang, X. Zhi, B. Johannessen, A. Slattery, S. Chern, S.-Z. Qiao, *Adv. Mater.* **2023**, *35*, 2209386.

[42] L. Jiao, J. Zhu, Y. Zhang, W. Yang, S. Zhou, A. Li, C. Xie, X. Zheng, W. Zhou, S. H. Yu, H. L. Jiang, *J. Am. Chem. Soc.* **2021**, *143*, 19417.

[43] Z. Yu, A. Si, A. P. LaGrow, Z. Tai, W. A. Caliebe, A. Tayal, M. J. Sampaio, J. P. S. Sousa, I. Amorim, A. Aeaujo, L. Meng, J. L. Faria, J. Xu, B. Liu, L. Liu, *ACS Catal.* **2022**, *12*, 9397.

[44] M. Tiwari, S. Gupta, R. Prakash, *RSC Adv.* **2014**, *4*, 25675.

[45] M. Shen, W. Yin, J. Li, H. Zhang, L. Chen, *J Mater Sci* **2018**, *29*, 13709.

[46] J. Li, Y. Liu, X. Tang, L. Xu, L. Min, Y. Xue, X. Hu, Z. Yang, *Mikrochim Acta* **2020**, *187*, 80.

[47] D. Y. Chung, H.-I. Kim, Y.-H. Chung, M. J. Lee, S. J. Yoo, A. D. Bokare, W. Choi, Y.-E. Sung, *Sci. Rep.* **2014**, *4*, 7450.

[48] T. Di, B. Zhu, B. Cheng, J. Yu, J. Xu, *J. Catal.* **2017**, *352*, 532.

[49] Y. Yang, Z. Chai, X. Qin, Z. Zhang, A. Muhetaer, C. Wang, H. Huang, C. Yang, D. Ma, Q. Li, D. Xu, *Angew. Chem., Int. Ed.* **2022**, *61*, e202200567.

[50] P. Liu, Z. Huang, X. Gao, X. Hong, J. Zhu, G. Wang, Y. Wu, J. Zeng, X. Zheng, *Adv. Mater.* **2022**, *34*, 2200057.

[51] Q. Zhao, L. Liu, S. Li, R. Liu, *Appl. Surf. Sci.* **2019**, *465*, 164.

[52] Y. Zhang, J. Zhao, H. Wang, B. Xiao, W. Zhang, X. Zhao, T. Lv, M. Thangamuthu, J. Zhang, Y. Guo, J. Ma, L. Lin, J. Tang, R. Huang, Q. Liu, *Nat. Commun.* **2022**, *13*, 58.

[53] P. Zhou, F. Lv, N. Li, Y. Zhang, Z. Mu, Y. Tang, J. Lai, Y. Chao, M. Luo, F. Lin, J. Zhou, D. Su, S. Guo, *Nano Energy* **2019**, *56*, 127.